Coupled weather research and forecasting–stochastic time-inverted lagrangian transport (WRF–STILT) model

Coupled Weather Research and Forecasting - Stochastic Time-Inverted Lagrangian Transport (WRF-STILT) Model

Thomas Nehrkorn

Atmospheric and Environmental Research, Inc., Lexington, Massachusetts, USA

Tel: 781-761-2288

Fax: 781-761-2299

Email: tnehrkor@aer.com

URL: www.aer.com

Janusz Eluszkiewicz

Atmospheric and Environmental Research, Inc., Lexington, Massachusetts, USA

Steven C. Wofsy

Harvard University, Cambridge, Massachusetts, USA

John C. Lin

University of Waterloo, Waterloo, Ontario, Canada

Christoph Gerbig

Max-Planck-Institut für Biogeochemie, Jena, Germany

Marcos Longo

Harvard University, Cambridge, Massachusetts, USA

Saulo Freitas

Center for Weather Forecasts and Climate Studies (CPTEC), INPE, Cachoeira Paulista, Brazil

This paper describes the coupling between a mesoscale numerical weather prediction model, the Weather Research and Forecasting (WRF) model, and a state-of-the-science Lagrangian Particle Dispersion Model, the Stochastic Time-Inverted Lagrangian Transport (STILT) model. The primary motivation for developing this coupled model has been to reduce transport errors in continental-scale top-down estimates of terrestrial greenhouse gas fluxes. Examples of the model's application are shown here for backward trajectory computations originating at CO_2 measurement sites in North America. Owing to its unique features, including meteorological realism and large support base, good mass conservation properties, and a realistic treatment of convection within STILT, the WRF-STILT model offers an attractive tool for a wide range of applications, including inverse flux estimates, flight planning, satellite validation, emergency response and source attribution, air quality, and planetary exploration.

1. Introduction

Ever since the pioneering work of Uliasz (1993), it has been recognized that the coupling of a Lagrangian Particle Dispersion Model (LPDM) to a numerical weather prediction (NWP) model offers the best tool for realistic atmospheric transport simulations on regional, continental and, under some circumstances, global scales. The Lagrangian approach, both in the forward and backward (receptor-oriented) mode (Seibert and Frank, 2004), is the method of choice when dealing with highly localized sources or receptors, while NWP models offer the most realistic wind fields with which to drive the LPDM. Current applications include air quality (Draxler and Hess, 1997), emergency response and source attribution (Buckley, 2000; Seibert and Frank, 2004), surface flux estimates (Flesch et al., 1995; Gerbig et al., 2003), validation and analysis of satellite data (Worden et al., 2007; Avey et al., 2007), and flight planning (Forster et al., 2004; Lin et al., 2007). Future applications may include biogenic source attribution on Mars, envisioned as motivation for the spacecraft missions planned for the next decade (Calvin et al., 2007).

In view of the recognized potential of coupled LPDM/NWP models and prompted by the Chernobyl disaster, several such models have been developed and are currently supported and extensively used. The availability of multiple models is highly beneficial, as a model-ensemble approach is a very promising way of reducing transport uncertainties in dispersion modeling (e.g., Galmarini et al., 2004). Of particular note are the Colorado State University LPDM coupled to the Regional Atmospheric Modeling System (RAMS) model (Uliasz, 1993; Cotton et al., 2003; Pielke et al., 1992; Buckley, 2000) and the FLEXPART model coupled to the European Centre for Medium-Range Weather Forecast (ECMWF) and the Weather Research and Forecasting (WRF) models (Stohl et al., 2005). A third coupled LPDM/NWP model, the Stochastic Time Inverted Lagrangian Transport (STILT) model coupled to the WRF model, forms the focus of this paper. The STILT model was originally developed for carbon science applications, but it should be attractive to a wide range of research and operational applications. Given its large existing and potential user base, we believe that a documentation

of the coupled WRF-STILT model, highlighting its unique aspects, will be helpful to the community. With this in mind, in this paper we will describe the numerical aspects of the coupling between the STILT and WRF models and present some general results demonstrating the performance of the coupled model, particularly with regard to mass conservation. Given that the WRF model is used extensively in both operational and research settings in the US and worldwide, this large support and user base assures that the coupled WRF-STILT model will "grow" with new advances in the LPDM and NWP fields.

2. WRF-STILT coupling

The STILT model, based on the HYSPLIT model developed at NOAA's Air Resources Laboratory (Draxler and Hess, 1997, 1998), is described in Lin et al. (2003), while the WRF model is described in Skamarock and Klemp (2008) and extensively documented in Skamarock et al. (2005). Consequently, in this section, we confine ourselves to describing those aspects of both models that are directly relevant to the coupling between them. This coupling utilizes concepts and approaches developed for the coupling between the STILT model and another widely used mesoscale model, the RAMS model in its Brazil implementation BRAMS (Brazilian RAMS) (Freitas et al., 2005, 2009; Medvigy et al., 2005). Recently, STILT has been coupled to ECMWF forecasts (Gerbig et al., 2008). Besides WRF, RAMS, and ECMWF, the STILT model is currently configured to be driven by meteorological fields produced by the National Centers for Environmental Prediction (NCEP) global and regional data assimilation systems. The ability of utilizing fields produced by different meteorological drivers allows for in-depth model intercomparison studies. The results presented in this paper have been obtained using version 2.1.2 of the Eulerian mass-coordinate dynamical core of WRF, which is part of the Advanced Research WRF supported by the National Center for Atmospheric Research (NCAR). As this version does not support nudging, we employed a series of overlapping 30-hour runs to produce continuous simulations for months at a time (see Section 3.1). More recent applications (see Section 4) have used version 2.2 (which includes nudging capabilities) and version 3.0.

2.1 STILT Model Grids

To minimize errors resulting from horizontal interpolation of model variables, the STILT model is designed to perform all computation on the horizontal grid of the meteorological input dataset. Currently supported map projections are conformal, including polar stereographic, Mercator, and Lambert (the latter has been used in the work described herein). By default, the code assumes that all model variables are located at the same mesh points, i.e., that there is no staggering of mass and momentum variables in the horizontal. Input datasets from models using staggered grids must thus be either interpolated to an unstaggered grid or special handling must be implemented within the STILT code whenever staggered variables (usually the horizontal wind components) are interpolated to trajectory locations. The latter approach is taken in STILT for the BRAMS and WRF model input.

The STILT/HYSPLIT models use a s vertical coordinate, defined as

(1)

where z_{top} is the model top height, z_{msl} is the height of the model level (above mean sea level, MSL), and z_{gl} is the height of the model terrain (above MSL). In the default mode, the STILT model uses a set of vertical coordinates values in which the grid level index k and model level height above ground for a gridpoint at MSL are related through a quadratic relationship (Draxler and Hess, 1997)

(2)

with a = 30 m, b = -25 m, and c = 5 m and z_{top} = 25 km. The default mode is employed when STILT is driven by pressure-level analyses, e.g., outside of the domain covered by WRF or another mesoscale model. For runs driven by WRF or ECMWF winds, the values of h are specified in a separate file, while for NWP models employing the s vertical coordinate, such as RAMS, their model levels are used directly in STILT.

2.2 STILT Input Variables

The most important meteorological variables required for trajectory calculations in STILT are vertical profiles of the horizontal and vertical wind components. The horizontal winds are assumed to be in m s^{-1} and are converted internally to grid lengths/minute, whereas the vertical velocity is converted from the meteorological input to its internal representation of ds/dt. In addition, profiles of temperature, pressure, and humidity are needed and converted internally to pressure, virtual potential temperature, relative humidity, and air density. Variables at the surface needed for the computation of sigma-level profiles are the terrain height, pressure, and temperature.

Additional two-dimensional fields are used for the determination of turbulence parameters (such as surface roughness length; latent and sensible heat flux at the surface; friction velocity). The height of the planetary boundary layer can be either computed internally in STILT, or provided as an input from the meteorological model. Other two-dimensional fields (such as radiative fluxes at the surface) are used in coupling the STILT output to biosphere models. Coupling of the convective parameterization within RAMS or WRF with the convective flux parameterization within STILT requires additional variables, as described in Section 2.7.

2.3 WRF Model Grids

The computational grid of the WRF model is regularly spaced in one of several possible map projections, including the STILT-supported conformal projections (polar stereographic, Mercator, and Lambert). A global latitude-longitude grid option is also available starting with version 3.0. These grids may be nested, but each nest is output separately and treated as a separate grid in STILT. The vertical coordinate used by the WRF model is a terrain-following pressure-sigma coordinate system based on the dry hydrostatic pressure p_{dh}. It is defined as

$$\eta = \frac{p_{dhs} - p_{dht}}{p_{dhs}}, \text{ where } \eta \qquad (3)$$

Here p_{dhs} and p_{dht} are the dry hydrostatic pressure at the surface and the model top, respectively. Note that the symbol η has been adopted by the WRF

developers for this coordinate system, although it is different from the traditional h coordinate (UCAR, 2000).

2.4 WRF Wind and Thermodynamic Variables

The standard output provided by the WRF model includes instantaneous values of the grid relative horizontal wind components (*u, v*) and the geometric vertical velocity dz/dt (all three components in m s^{-1}) at the staggered grid locations of the Arakawa C-grid (Arakawa and Lamb, 1977). The WRF-STILT interface provides the option to use these velocities, in which case only minor changes are required to the WRF model code.

The WRF model equations are formulated as perturbation equations with respect to a dry hydrostatic reference state at rest. Thermodynamic quantities available in the standard WRF model output include the (full or perturbation) potential temperature, the base state and perturbation pressure, and the water vapor mixing ratio. Additional WRF model variables are required by the WRF-STILT interface to permit computation of the WRF model level heights (see Section 2.1). They include the dry inverse density a_d, needed for the integration of the WRF hydrostatic equation

(4)

and the base state and perturbation values of μ_d.

2.5 WRF Mass-Coupled Wind Variables

Aside from the accuracy of the meteorological fields, an important requirement for the meteorological input fields for an LPDM is that they conserve mass (Lin et al., 2003). While the WRF and other NWP models usually conserve mass internally to a high degree, this can no longer be guaranteed if the model variables are transformed and temporally and spatially interpolated (by the NWP model's postprocessing and/or the LPDM's preprocessing routines). To minimize these problems, the WRF-STILT interface provides the option to make use of time-averaged values of the mass-coupled velocities used internally by WRF for the

advection of passive scalars. The mass-coupled horizontal velocities (*U, V*) are defined as

, (5)

where (*u, v*) are the grid-relative wind components, and *m* is the map scale factor. A coupled vertical velocity is similarly defined as

(6)

The time stepping used in the WRF model for the slow (non-acoustic) modes is a third-order Runge-Kutta scheme. Acoustic tendencies are stepped on a shorter time step, using deviations from the last large time step values of the Runge-Kutta scheme. Passive scalars are advected using values of *U, V*, and Ω that are time-averaged over the acoustic steps. For use by the STILT model, *U, V*, and Ω are further averaged over all large time steps within the output interval of the WRF model (this is a user-specified parameter; experiments reported here used an interval of 1 hour).

2.6 Vertical Interpolation and Variable Transformation

In order to utilize WRF fields, the STILT source code primarily required modifications in its meteorological input module and in the interpolation of the input profiles to the STILT model levels. Additional changes, which are not described in detail here, were required throughout a number of modules to account for the horizontal and vertical staggering of the wind components, and the treatment of time-averaged rather than instantaneous model values. Both of these aspects are quite similar to the provisions for the RAMS model input.

The meteorological input module was modified to process the required and optional WRF model fields. Base state and perturbation quantities of pressure and η are combined to full values in this module. In order to perform the vertical interpolation from WRF to STILT model levels, the height above terrain of the STILT *k*-th model level is first computed using Equation (1)

(7)

The corresponding height above ground for the input WRF mass model levels is obtained by upward integration of Equation (4)

(8)

where is the spacing of the WRF mass levels, and $\bar{a}_d$ is the layer-average value of a_d, computed from the mass level values as in Skamarock et al. (2005, Equation (3.28)). The WRF mass level model variables are then interpolated linearly in height from the WRF mass levels to the STILT model levels.

2.7 Accounting For Convection in STILT

Modern LPDMs account for the impact of convective motions on particle dispersion (e.g., Forster et al., 2007). In its original implementation, the STILT model either ignored the impact of convective motions on the trajectory calculations or treated them in a simplistic way to create an upper bound by vertically mixing throughout the entire unstable layer (defined by the limit of convection) diagnosed at each meteorological input time (Gerbig et al., 2003). The availability in both the RAMS and WRF models of convective mass fluxes, parameterized using the Grell et al. (1994) or Grell and Devenyi (2002) schemes, allows for a more sophisticated approach, in which the STILT model takes detailed account of convective mass fluxes in the dispersion of particles, incorporating the vertical profiles of up- and downdrafts, and detrainment and entrainment fluxes between the environment and convective elements. This scheme, originally for the STILT/BRAMS coupling, extends the method described by Freitas et al. (2000). A distinguishing aspect of this scheme is that it directly uses the convective mass fluxes generated by the NWP model in a stochastic fashion (particle has a higher probability by a specific mass flux, with probability in direct proportion to the magnitude of the mass flux), and the WRF and BRAMS models have been modified to output them in a format compatible with STILT.

2.7.1 Convective Fluxes in WRF

In the WRF model, the Grell-Devenyi scheme (Grell and Devenyi, 2002) is implemented for deep convection only (shallow convection is not yet implemented). The scheme uses a 144-member ensemble of parameterizations,

allowing for 3 different values of precipitation efficiency, 3 different values for a numerical parameter related to the cloud base mass flux normalization, and 16 different closure assumptions. Within the scheme, all computed convective fluxes are normalized by the cloud base mass flux. The normalized fluxes are averaged over the ensemble members, and then scaled by the ensemble-averaged cloud base mass flux.

The Grell-Devenyi scheme is a mass-flux scheme, in which the grid-cell average of the updraft mass flux profile is given by

(9)

where l denotes the ensemble member, m_b is the mass-flux at cloud base, and h_u is the normalized updraft mass flux profile. Similarly, the downdraft mass flux is given by

(10)

where m_o is the mass flux at the originating level of the downdraft. m_o is related to the cloud base mass flux m_b through a parameter e that depends on the precipitation efficiency 1 , the total condensation in the updraft I_1, and the evaporation in the downdraft I_2 (Grell, 1993, Equation (A.24))

(11)

The vertical profiles of the normalized up- and downdraft mass fluxes are controlled by the fractional entrainment and detrainment rates, which are then used to arrive at the final values of entrainment and detrainment rates based on additional assumptions about entrainment and detrainment at the top and bottom of the up- and downdrafts. The entrainment and detrainment mass fluxes are used for the computation of convectively induced tendencies of the environment. Details of this computation, and the mass budget of the convective fluxes, are shown in Grell (1993, Figure B1). An internal consistency check for mass conservation is included in the scheme.

2.7.2 Convective Fluxes Within STILT

For the Grell-type convection schemes, STILT uses vertical profiles of the mass flux within the updrafts and downdrafts, and the entrainment of mass from the environment into the up- and downdrafts (and detrainment into the environment from the up- and downdrafts). It is assumed that the up- and downdraft mass fluxes (in kg m^{-2} s^{-1}) are given at the staggered model levels, while the entrainment and detrainment fluxes (also in kg m^{-2} s^{-1}) are defined at mass levels, representing the change in up- or downdraft mass flux over the layer depth due to entrainment and detrainment. The grid-cell averages of up- and downdraft mass fluxes at cloud base are converted to a fractional coverage, using the square root of TKE as updraft velocity (with the PBL scheme used in the experiments reported here, TKE is not available from the WRF output, and an assumed value of 1 m s^{-1} is used instead). Vertical profiles of up- and downdraft vertical velocity are then derived from the flux profiles and the (vertically constant) fractional coverage of the up- and downdrafts. The vertical profiles of the up- and downdraft mass fluxes, and their changes due to entrainment and detrainment, are used to compute the probability of individual particles being located within the environment or in an up- or downdraft.

Rigorous tests to ensure adherence to the well-mixed criterion were conducted during the development and implementation of the convective scheme in STILT. The well-mixed criterion is a physical principle that states particles in a LPDM should maintain a well-mixed distribution that follows the profile of atmospheric density, a direct consequence of the second law of thermodynamics (Thomson, 1987). Tests involved large ensembles of 10,000 particles, initially well mixed in the vertical, with their convective motion integrated over long times (up to several weeks) in real convective cases to ensure well-mixedness within the column.

To support the use of WRF-generated convective mass fluxes, changes were needed in the computation of the vertical levels passed to the Grell convection subroutine in STILT, since the existing RAMS implementation assumed that the fluxes were available at the staggered vertical grid of the RAMS model data. In addition, the vertical interpolation routine for WRF input data had to be augmented to support a remapping of the mass fluxes to the STILT model levels.

As was the case for the vertical velocity, the wind-level up- and downdraft mass fluxes are interpolated to the staggered STILT levels, while the entrainment and detrainment fluxes are redistributed to the STILT layers.

3. Sample Results

The WRF-STILT interface has been extensively used during CO_2 simulations over the Northeastern United States. The experimental setup for these simulations is described in the next section, followed by a discussion of selected results that illustrate general aspects of the WRF-STILT model, including mass conservation and sensitivity to model resolution and the treatment of convection. Additional applications are discussed in Section 4.

3.1 Experimental Setup

The results presented in this paper were obtained using version 2.1.2 of the Advanced Research WRF (ARW) (Skamarock et al., 2005), with the following physics options:

- Radiation: RRTM scheme (Mlawer et al., 1997) for the longwave and Goddard scheme (Chou and Suarez, 1994) for the shortwave.
- Planetary Boundary Layer: Yonsei University (YSU) scheme coupled with the NOAH land surface model and the MM5 similarity theory based surface layer scheme.
- Microphysics: Purdue Lin scheme (Lin et al., 1983; Chen and Sun, 2002).
- Convection: Grell-Devenyi ensemble mass flux scheme (Grell and Devenyi, 2002).

The selected radiation schemes are generally considered the most accurate choices available in version 2 of WRF. The YSU PBL scheme was found by Fast (2005) to perform better in estimating the height of the PBL than higher moment schemes. The choice of the microphysics scheme is consistent with that of Fast (2005), while the choice of the cumulus convection scheme enabled us to include the computed convective mass fluxes in the meteorological input fields for STILT, as described in Section 2.7.

The outer model domain with a grid resolution of 40 km was chosen to cover most of the continental North America using a Lambert conformal projection (see

Figure 1). In addition, a nested domain with 8-km grid resolution was placed over the Argyle tower location in Maine (45.03˚N, 68.68˚W), using one-way nesting. All runs described here used 30 levels. Model results were output hourly. North American Regional Reanalysis fields (NARR, Mesinger et al., 2006) were used for initial and lateral boundary condition data. The NARR fields are generated using the NCEP regional data analysis system (EDAS), and are available on a 32-km Lambert conformal grid. A series of free-running forecasts were used to generate continuous meteorological fields for May through September of 2004. Each forecast was started at 00 UTC, and hours 6 – 30 of the forecast were used (thus avoiding spin-up artifacts and other transients during the first 6 hours).

3.2 Verification of Meteorological Fields

For a statistical evaluation, we compute verification statistics both against radiosonde observations and gridded analysis fields. The set of radiosonde observations used in this analysis is shown in Figure 2. The comparison against the radiosondes uses the STILT trajectory model: for each station location, observation level, and time, the trajectory model is run for a brief integration time, and the corresponding zonal and meridional displacements are then compared against the observed zonal and meridional winds. This approach, while computationally slow, has the advantage that it directly uses the ARL-formatted input meteorological files used by STILT, and can thus be directly applied to any of the various meteorological inputs compatible with STILT, regardless of what grid structure or model variables are used. It also provides a test of the way the meteorological information is actually used in the trajectory model.

A comparison of the WRF fields against gridded analysis allows a more detailed examination of the evolution of the forecast error with lead-time, and of its dependence on vertical level. For a densely sampled region like the North American continent, radiosonde observations still constitute the most important data source for the analysis, although other observations and information propagated by the forecast model may lead to non-trivial differences. For the area of the Northeast US bounded by the outer green box in Figure 2, error statistics were accumulated for all NARR analysis grid points contained within this box.

The grid-point statistics used (instantaneous, not time-averaged) WRF model results interpolated in space to the analysis grid points.

Sample statistics obtained using both methods (using all the stations and grid points within the outer green box in Figure 2) are shown in Figure 3 for a total of 32 forecasts between June 1 and July 10, 2004. Results are shown separately for forecast valid times at 12 UTC (this corresponds to a 12-hour forecast for the WRF fields) and 00 UTC (corresponding to a 24-hour WRF forecast). As expected, the WRF errors are larger at the 24-hour forecast lead-time than at 12 hours. The gridded error statistics show generally smaller error magnitudes than those based on radiosondes, but they show the same qualitative dependence on level and forecast lead-time. It is unclear whether the differences are due to the differences in the verification procedure, the fact that the verifying analyses are also used as initial and boundary conditions for the WRF forecast (however, given the size of the outer WRF domain, the influence of the lateral boundary conditions is not likely a major factor at 12 and 24 hours into the forecast), or simply the result of sampling differences.

A more complete picture of the forecast error growth over the entire 30-hour forecast length is shown in Figure 4. Lin et al. (2007) found qualitatively similar error growth of forecast winds compared to radiosonde observations for mesoscale models during May/June 2003 (because of differences in averaging, results are not directly comparable). In more recent work (Section 5), nudging of the forecast to gridded analyses was used to limit this error growth.

Radiosonde verification statistics were also computed for the WRF fields from the inner domain, for the same dates and times as shown in Figure 3 (gridded verification statistics were not computed for the inner domain, since the verifying analysis is only available at a coarser resolution). The results are shown in Figure 5. For comparison, the error statistics for the coarse resolution WRF forecasts, computed for the same times and radiosondes, are also shown Figure 5. There is no clear benefit of using higher horizontal resolution in terms of these statistics, with smaller errors at some levels (400 and 300 hPa), and larger errors at others

(850 hPa). However, there are cases where using nested fields has a large effect on simulated trajectories, as is shown in the next section.

3.3 Trajectory Results

One of the motivations for using the WRF model fields was that it is possible to include nested domains with increased resolution near the receptor site, where the details of the smaller-scale circulations can play an important role in the simulated trajectories. The effect of using nested vs. coarse-resolution input fields on the resulting trajectories is particularly dramatic for the case shown in Figure 6 (back trajectories starting at 23 UTC on June 23, 2004). A substantial number of trajectories computed using coarse-resolution fields approach the Argyle tower from the South and Southeast, abutting the coastline, whereas the higher resolution fields result in trajectories that approach straight from the West. The synoptic situation for this case is characterized by a weak surface low with a trough line extending northward into Maine. There are important differences in how this feature is resolved in the coarse and nested WRF model output fields, which results in low-level flow from the North at Argyle in the nested WRF output, and a flow more from the East in the coarse-resolution WRF fields. An additional factor causing differences in the trajectories is that the nested WRF fields have much stronger vertical velocities (not shown here), resulting in a much larger proportion of particles at higher levels in the nested run, where winds are predominantly from the west.

The effects of including the convective mass fluxes in the trajectory calculations are generally small for the mid-latitude surface locations we have examined. A case that did show some sensitivity was for a receptor at the Argyle location on 18 UTC July 16, 2004. Figure 7 shows results for the 30-hour back trajectories in this case. As is evident from the top left panel, the vertical distribution of the particles from trajectory computations with and without convective mass fluxes begin to diverge after 18 hours, i.e. at 00 UTC. An examination of the 6-hour period between 24 and 30 hours backward trajectory time (12 to 18 UTC on July 15) shows the particles in an area of convective activity predicted by the WRF model. The spatial distribution and magnitude of the WRF-predicted convective precipitation agrees well with the corresponding Stage IV precipitation analysis in

this case. Stage IV precipitation analyses, which are produced operationally by River Forecast Centers and mosaiced into a national 4-km resolution grid by the National Centers for Environmental Prediction (NCEP), are based on multi-sensor precipitation analyses combining radar precipitation estimates, raingauge data, and manual quality control (additional information is available at *http://www.emc.ncep.noaa.gov/mmb/ylin/pcpanl/*).

The impact on the trajectory locations is too small to be readily apparent in the plot of particle positions shown in Figure 7. A more relevant measure related to the sensitivity of simulated CO_2 concentration on surface fluxes is the "footprint". As defined in Lin et al. (2003), it provides the concentration change (in parts per million, ppm) at the receptor for a unit surface flux (in μmol $m^{-2}s^{-1}$) persisting over a given time interval; its units are ppm $\mu mol^{-1}m^2s$. A plot of the footprints for the same 6-hour time period as in Figure 7 is shown in Figure 8. The effect is small, but not negligible, in this case.

3.4 Mass Conservation

As discussed in Section 2.5, spatial and temporal interpolations of model fields and variable transformations from the variables used in the NWP model to those used in the LPDM can lead to fields that no longer conserve mass, particularly when instantaneous wind fields are used. To diagnose the lack of mass conservation in the meteorological input fields (and apply a first order correction), the cumulative mass violation is tallied within STILT for each particle (Lin et al., 2003). To test the degree to which mass is conserved using WRF fields, two-day back trajectories were computed from the Argyle tower for six arbitrarily chosen times in July (08 UTC July 08, 15 UTC July 11, 22 UTC July 14, 05 UTC July 18, 12 UTC July 21, 19 UTC July 24), using 1000 particles each. The distribution of the cumulative fractional change in mass *dmass* (equal to 1 for perfect mass conservation, and equal to 0.5 for a 50% loss of mass) is shown in Figure 9 for trajectories computed using the outer domain WRF fields, using either time-averaged flux quantities or instantaneous winds, and using global NCEP analysis fields. Using time-averaged fluxes results in much better mass-conservation properties of the interpolated wind fields, with WRF fields going from being worse than the global analysis fields to being noticeably better.

By design, the *dmass* diagnostic only tests the mass conservation properties of the gridded component of the total wind field driving the trajectory calculations. A more comprehensive test of mass conservation, involving both the gridded and the stochastic components, is given by the well-mixed criterion (see Section 2.7.2). Violations of the well-mixed criterion cause unphysical accumulations of particles in low turbulence regions or at boundaries, leading to erroneous simulations of tracer concentrations. Our implementation of this test, based on explicit forward and backward trajectories, follows the procedure outlined by Lin et al. (2003). The backward trajectories used for Figure 9 were used to define a source region for the receptor location. The source region was then subdivided into longitude-latitude boxes, and an equally sized box was placed around the Argyle receptor location. Back trajectories were then computed for a total of 15,000 particles, using receptor locations randomly placed within a three-dimensional receptor box of 100-meter depth centered at the Argyle tower height of 107 m above ground. For each of the previously identified source boxes (further subdivided into 100 meter vertical intervals from 0 to 1 km) with a minimum of 10 particles originating from it, forward trajectories were then computed, using 15,000 particles from randomly chosen location inside the source box. For perfect adherence to the well-mixed criterion, the number of particles found to originate from the source box in the back trajectories would be equal to the number of particles in the forward trajectories that arrive in the receptor box. A scatterplot of corresponding forward and backward trajectory particle counts is shown in Figure 10 for the WRF outer domain instantaneous winds and time-averaged flux fields. Also shown are the results for the operational NCEP global analysis fields (also referred to as "FNL"). Both sets of trajectories computed using instantaneous winds have large scatter and small correlation coefficients, with significantly better correlations for the WRF time-averaged flux fields (the 95%-confidence intervals for the correlation coefficients are (0.36,0.46) for the analysis and WRF winds trajectories, and (0.69,0.75) for the WRF flux trajectories). The slope of the regression lines is also closer to the perfect slope for the WRF flux trajectories. These results thus confirm the conclusion reached from the analysis of the *dmass* diagnostic, that the use of time-averaged flux fields from WRF is crucial for mass-conserving LPDM trajectory computations.

4. Summary and Future Work

A description of the coupled WRF-STILT Lagrangian particle mesoscale modeling system is provided, and its performance is illustrated for a carbon budget study over the North American continent. The use of (nonstandard) time-averaged, mass-coupled velocity fields from the WRF model was found to be crucial in improving the mass conservation properties of the coupled modeling system. Sensitivity to other aspects of the mesoscale model fields, such as the use of high-resolution nested domains and the inclusion of convective fluxes, was found to be highly case dependent. Since uncertainties due to transport errors can have a large impact on carbon budget computations and inferred source strengths (Gerbig et al., 2008; Gloor et al., 1999; Lin and Gerbig, 2005), this suggests that a case-dependent evaluation of the sensitivities and associated uncertainties may be needed for these applications.

The WRF-STILT modeling system has been applied to a number of other applications. To support the top-down estimates of surface fluxes of CO_2 and other greenhouse gases from available tower and aircraft measurements of trace gas concentrations, multi-year simulations at a resolution of 10km, and down to 2km for selected tower locations, have been generated for the North American continent (Michalak et al. 2007) using version 2.2 of WRF with nudging to the NARR analysis. WRF-STILT has been used for estimates of methane fluxes by Kort et al. (2008) and Zhao et al. (2009), with additional efforts underway for an expanded analysis of non-CO_2 greenhouse gas emissions (e.g., http://nacp.ornl.gov/mast-dc/int_synth_greenhouse.shtml).

Current work continues on both the WRF and STILT models. As a community model, WRF continues to evolve with added capabilities and improved parameterization packages being added continually. Of particular interest to modeling of the carbon cycle are efforts to improve the radiative transfer computations. For example, Iacono et al. (2009) evaluated the effect of introducing a new radiation package into WRF version 3.1 (RRTMG, Iacono et al. 2008), and documented small but consistent improvements in the short-wave flux incident at the surface, a critical parameter for modeling the biospheric uptake of CO_2 by photosynthesis.

The software for the WRF-STILT modeling system is available from the first author.

5. Acknowledgements

Work at AER has been supported by the NASA Terrestrial Ecology Program and the National Science Foundation Atmospheric Chemistry Program.

6. References

Arakawa, A. and V. Lamb, 1977: Computational design of the basic dynamical processes of the UCLA general circulation model. In *Methods in Computational Physics*, volume 17, pages 174-267. Academic Press.

Avey, L., T. J. Garrett, and A. Stohl, 2007: Evaluation of the aerosol indirect effect using satellite, tracer transport model, and aircraft data from the International Consortium for Atmospheric Research on Transport and Transformation, *J. Geophys. Res., 112,* D10S33, doi:10.1029/2006JD007581.

Buckley, R. L., 2000: Modeling atmospheric deposition from a cesium release in Spain using a stochastic transport model, *11th Joint Conference on the Applications of Air Pollution Meteorology with the Air and Waste Management Association*, Long Beach, CA, American Meteorological Society, 190-195.

Calvin, W. et al., 2007: Report from the 2013 Mars Science Orbiter (MSO) Second Science Group, 72 pp., posted June 2007 by the Mars Exploration Program Analysis Group (MEPAG) at http://mepag.jpl.nasa.gov/reports/index.html.

Chen, S.-H. and W.-Y. Sun, 2002: A one-dimensional time dependent cloud model. *J. Meteor. Soc. Japan*, 80 (1), 99–118.

Chou, M.-D. and M. Suarez, 1994: An efficient thermal infrared radiation parameterization for use in general circulation models. Tech. Memo. 104606, NASA, Washington, DC.

Cotton, W. R., et al., 2003: RAMS 2001: Current status and future directions, *Meteorol. Atmos. Phys.,* 82, 5-29.

Draxler, R. R., and G. D. Hess, 1997: Description of the HYSPLIT_4 modeling system, NOAA Tech. Memo. ERL ARL-224, 24 pp.

Draxler, R. R. and G. D. Hess, 1998: An overview of the HYSPLIT_4 modeling system for trajectories, dispersion, and deposition, *Aust. Meteorol. Mag., 47,* 295-308.

Fast, J. D., 2005: Evaluation of the boundary layer characteristics and particulates in Mexico City predicted by WRF. *Joint WRF/MM5 Users' Workshop*, NCAR, Boulder, CO, available from http://www.wrf-model.org/wrfadmin/presentations.php.

Flesch, T. K., Wilson, J. E., and Yee, E., 1995: Backward-time Langrangian stochastic dispersion models and their application to estimate gaseous emissions, *J. Appl. Meteor., 34,* 1320–1332.

Forster, C., et al., 2004: Lagrangian transport model forecasts and a transport climatology for the Intercontinental Transport and Chemical Transformation 2002 (ITCT 2K2) measurement campaign, *J. Geophys. Res., 109,* D07S92, doi:10.1029/2003JD003589.

Forster, C., A. Stohl, and P. Seibert, 2007: Parameterization of convective transport in a Lagrangian particle dispersion model and its evaluation, *J. Appl. Meteor. Clim., 46,* 403-422.

Freitas, S. R., M. A. F. Silva Dias, P. L. Silva Dias, K. M. Longo, P. Artaxo, M. O. Andreae, and H. Fisher, 2000: A convective kinematic trajectory technique for low-resolution atmospheric models, *J. Geophys. Res., 105(D19),* 24,375-24,386.

Freitas, S. R., K. M. Longo, M. A. F. Silva Dias, P. L. Silva Dias, R. Chatfield, E. Prins, P. Artaxo, G. Grell, and F. S. Recuero, 2005: Monitoring transport of biomass burning emissions in South America, *Environ. Fluid Mech., 5,*135-167.

Freitas, S. R., K. M. Longo, M. A. F. Silva Dias, R. Chatfield, P. Silva Dias, P. Artaxo, M. O. Andreae, G. Grell, L. F. Rodrigues, A. Fazenda, and J. Panetta, 2009: The Coupled Aerosol and Tracer Transport model to the Brazilian developments on the Regional Atmospheric Modeling System (CATT-BRAMS) – Part 1: Model description and evaluation, *Atmos. Chem. Phys., 9,* 2843-2861.

Galmarini, S., R. Bianconi, W. Klug, T. Mikkelsen, R. Addis, S. Andronopoulos, P. Astrup, A. Baklanov, J. Bartniki, J. C. Bartzis, R. Bellasio, F. Bompay, R. Buckley, M. Bouzom, H. Champion, R. D'Amours, E. Davakis, H. Eleveld, G. T. Geertsema, H. Glaab, M. Kollax, M. Ilvonen, A. Manning, U. Pechinger, C. Persson, E. Polreich, S. Potemski, M. Prodanova, J. Saltbones, H. Slaper, M.A. Sofiev, D. Syrakov, J.H. Sørensen, L. Van der Auwera, I. Valkama, and R. Zelazny, 2004: Ensemble dispersion forecasting – Part I: concept, approach and indicators, *Atmos. Environ., 38,* 4607-4617.

Gerbig, C., S. Korner, and J.C. Lin, 2008: Vertical mixing in atmospheric tracer transport models: error characterization and propagation. *Atmos. Chem. Phys.,* 8, 591-602.

Gerbig, C., J. C. Lin, S. C. Wofsy, B. C. Daube, A. E. Andrews, B. B. Stephens, P. S. Bakwin, and C. A. Grainger, 2003: Towards constraining regional scale fluxes of CO_2 with atmospheric observations over a continent: 2. Analysis of COBRA data using a receptor-oriented framework, *J. Geophys. Res., 108* (D24), 4757, doi:10.1029/2003JD003770.

Gloor, M., S.-M. Fan, S. Pacala, J. Sarmiento, and M. Ramonet,1999: A model-based evaluation of inversions of atmospheric transport, using annual mean mixing ratios, as a tool to monitor fluxes of nonreactive trace substances like CO_2 on a continental scale, *J. Geophys. Res.*, *104* (D12), 14,245-14,260.

Grell, G., 1993: Prognostic evaluation of assumptions used by cumulus parameterizations, *Mon. Wea. Rev., 121,* 764– 787.

Grell, G. A. and D. Devenyi, 2002: A generalized approach to parameterizing convection combining ensemble and data assimilation techniques, *Geophys. Res. Lett., 29,* 1693, doi:10.1029/2002GL015311.

Grell, G. A., J. Dudhia, and D. R. Stauffer, 1994: A description of the fifth generation Penn State/NCAR mesoscale model (MM5), *NCAR/Tech. Note-398+STR,* pp. 64-72, Natl. Cent. For Atmos. Res., Boulder, Colo.

Iacono, M. J., J. S. Delamere, E. J. Mlawer, M. W. Shephard, S. A. Clough and W. D. Collins, 2008: Radiative forcing by long-lived greenhouse gases: Calculations with the AER radiative transfer models, *J. Geophys. Res.,* 113, D13103, doi:10.1029/2008JD009944.

Iacono, M. J., T. Nehrkorn, J. Dudhia, and W. Wang, 2009: Application of RRTMG/McICA to the Advanced Research WRF weather forecast model. *Proceedings, 19th ARM Science Team Meeting*, Office of Science, U.S. Department of Energy, Louisville, KY, available from http://www.arm.gov/publications/proceedings/conf19/display.php?id=NTky.

Kort, E. A., J. Eluszkiewicz, B. B. Stephens, J. B. Miller, C. Gerbig, T. Nehrkorn, B. C. Daube, J. O. Kaplan, S. Houweling, and S. C. Wofsy, 2008: Emissions of CH4 and N2 O over the United States and Canada based on a receptor-oriented modeling framework and COBRA-NA atmospheric observations. *Geophys. Res. Lett.,* 35, L18 808, doi:10.1029/2008GL034 031.

Lin, J. C. and C. Gerbig, 2005: Accounting for the effect of transport errors on tracers inversions, *Geophys. Res. Lett., 32,* L01802, doi:10.1029/2004GL021127.

Lin, J. C., C. Gerbig, S. C. Wofsy, B. C. Daube, A. E. Andrews, K. J. Davis, and C. A. Grainger, 2003: A near-field tool for simulating the upstream influence of atmospheric observations: The Stochastic Time-Inverted Lagrangian Transport (STILT) model, *J. Geophys. Res., 108(D16),* 4493, doi:10.1029/2002JD003161.

Lin, J.C., C. Gerbig., S.C. Wofsy, R. Draxler, V.Y. Chow, and E.W. Gottlieb. Designing Lagrangian experiments to measure regional-scale trace gas fluxes, 2007: *J. Geophys. Res.*, *112* (D13312), doi:10.1029/2006JD008077

Lin, Y.-L., R. D. Farley, and H. D. Orville, 1983: Bulk parameterization of the snow field in a cloud model. *J. Appl. Meteor.,* 22 (6), 1065–1092.

Medvigy, D., P. R. Moorcroft, R. Avissar, and R. L. Walko, 2005:, Mass conservation and atmospheric dynamics in the Regional Atmospheric Modeling System (RAMS), *Environ. Fluid Mech., 5,* 109-134.

Mesinger, F., G. DiMego, E. Kalnay, K. Mitchell, P. C. Shafran, W. Ebisuzaki, D. Jovic, J. Woollen, E. Rogers, E. H. Berbery, M. B. Ek, Y. Fan, R. Grumbine, W. Higgins, H. Li, Y. Lin, G. Manikin, D. Parrish, and W. Shi, 2006: North American Regional Reanalysis. *Bull. Amer. Meteor. Soc.*, 87 (3), 343–360.

Michalak, A. M., K. Mueller, S. Gourdji, A. I. Hirsch, A. E. Andrews, J. C. Lin, and T. Nehrkorn, 2007: Bridging across spatial and temporal scales in North American carbon dioxide flux estimation through geostatistical analysis of scale-dependent relationships between carbon flux and auxiliary environmental data. *EOS, Trans. Amer. Geophys. Union*, 88 (52), Fall Meet. Suppl., Abstract B42C-01.

Mlawer, E. J., S. J. Taubman, P. D. Brown, M. J. Iacono, and S. A. Clough, 1997: Radiative transfer for inhomogeneous atmospheres: RRTM, a validated correlated-k model for the longwave. *J. Geophys. Res.,* 102 (D14), 16 663–16 682.

Pielke, R. A., et al., 1992: A comprehensive meteorological modeling system – RAMS, *Meteorol. Atmos. Phys., 49,* 69-91.

Seibert, P. and A. Frank, 2004: Source-receptor matrix calculation with a Lagrangian particle dispersion model in backward mode, *Atmos. Chem. Phys., 4,* 51-63.

Skamarock, W. C. and J. B. Klemp, 2008: A time-split nonhydrostatic atmospheric model for weather research and forecasting applications, *J. Comp. Phys., 227,* 3465-3485.

Skamarock, W. C., J. B. Klemp, J. Dudhia, D. O. Gill, D. M. Barker, W. Wang, and J. G. Powers, 2005: A description of the advanced research WRF version 2. Technical Note 468+STR, MMM Division, NCAR, Boulder, CO, 88 pp. Available from http://www.mmm.ucar.edu/wrf/users/docs/arw_v2.pdf.

Stohl, A., C. Forster, A. Frank, P. Seibert, and G. Wotawa, 2005: Technical Note: The Lagrangian particle dispersion model FLEXPART version 6.2, *Atmos. Chem. Phys., 5, 2461-2474*.

Thomson, D.J., 1987: Criteria for the selection of stochastic models of particle trajectories in turbulent flows, *Journal of Fluid Mechanics, 180*, 529-556.

UCAR, 2000: http://www.meted.ucar.edu/nwp/9cu1/ic2/frameset.htm?opentopic(2) Vertical Coordinates.

Uliasz, M, 1993: The atmospheric mesoscale dispersion modeling system (MDMS), *J. Appl. Meteor., 32,* 139-149.

Worden, H. M., J. A. Logan, J. R. Worden, R. Beer, K. Bowman, S. A. Clough, A. Eldering, B. M. Fisher, M. R. Gunson, R. L. Herman, S. S. Kulawik, M. C. Lampel, M. Luo, I. A. Megretskaia, G. B. Osterman, and M. W. Shephard, 2007: Comparisons of Tropospheric Emission Spectrometer (TES) ozone profiles to ozonesondes: Methods and initial results, *J. Geophys. Res.,* 112, D03309, doi:10.1029/2006JD007258.

Zhao, C., A. E. Andrews, L. Bianco, J. Eluszkiewicz, A. Hirsch, C. MacDonald, T. Nehrkorn, and M. L. Fischer, 2009): Atmospheric inverse estimates of methane emissions from Central California, *J. Geophys. Res.,* doi:10.1029/2008JD011671 (accepted, available at http://calgem.lbl.gov/worldview/CALGEM/Papers/Zhao-JGR-2008JD011671-CH4-Central-CA-final.pdf).

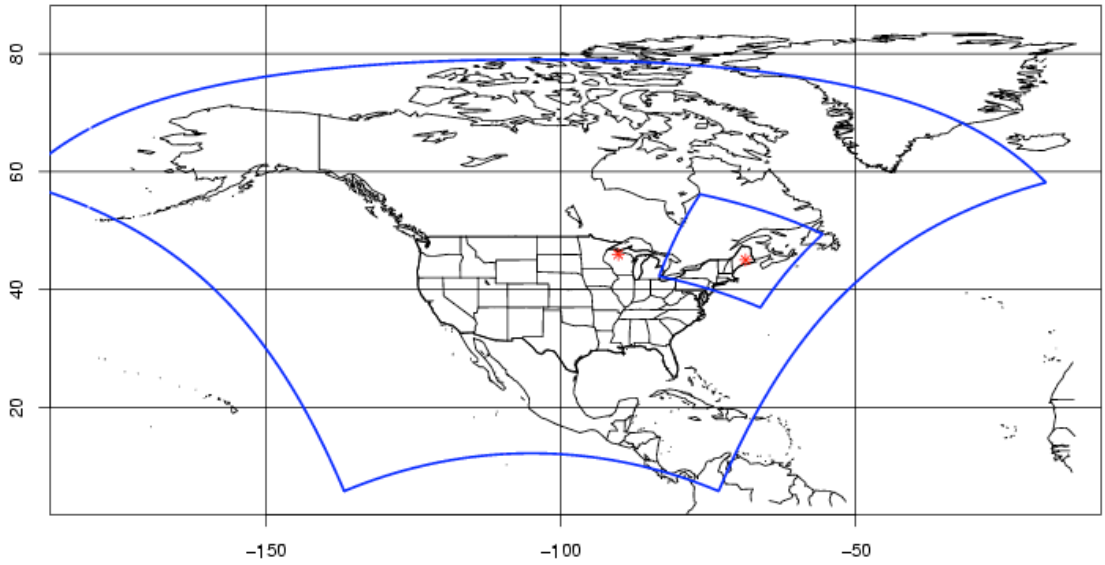

Fig. 1: WRF domains. Shown in red are the locations of two measurement sites: the Argyle tower in Maine and the WLEF tower in Park Falls, Wisconsin.

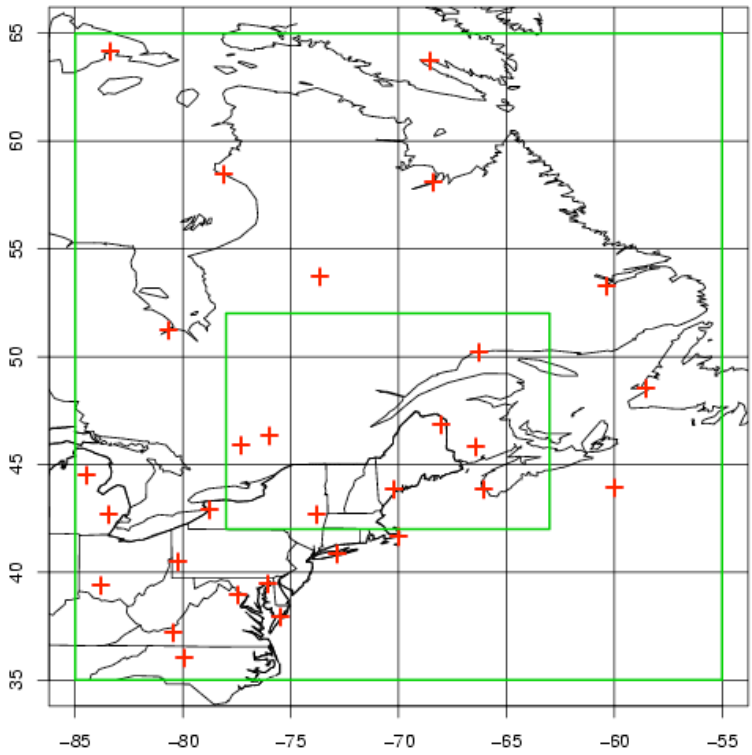

Fig. 2: Radiosonde locations used in the verification statistics. Green outlines denote longitude-latitude limits for grid points used in the gridded verification statistics, referred to as the Northeast US (outer green box) and inner domain (inner green box).

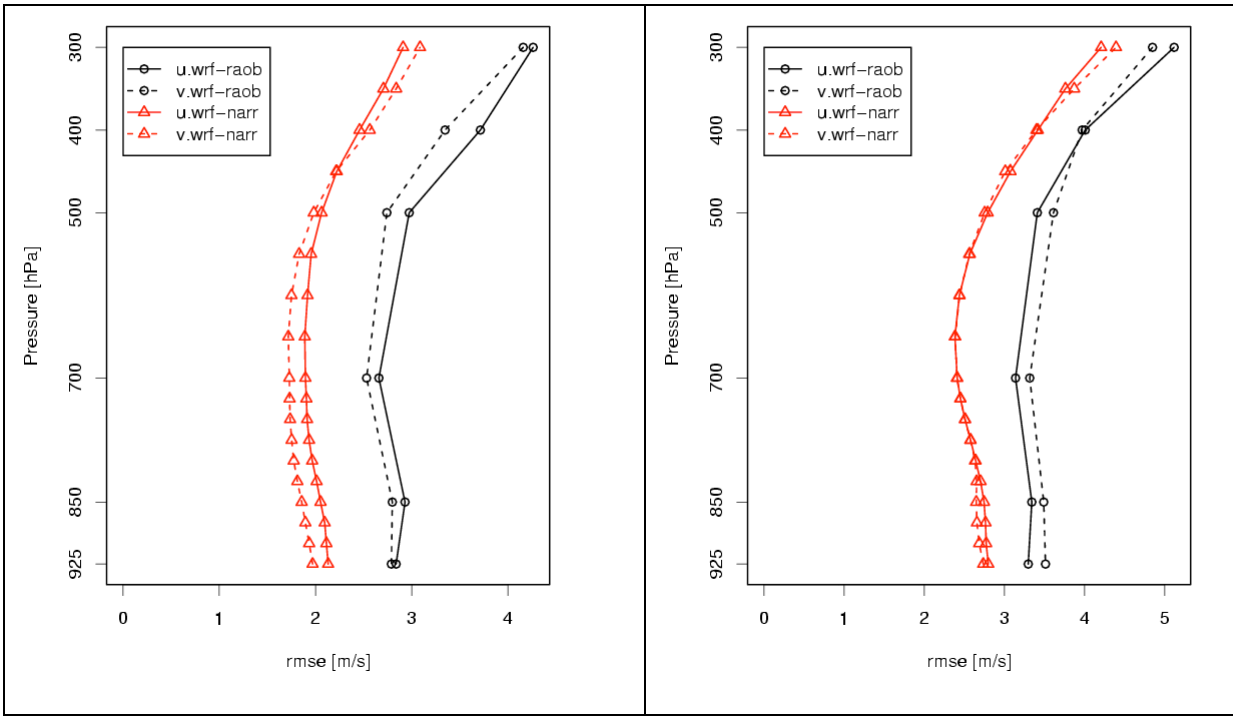

Fig. 3: Verification statistics for WRF forecasts valid at 12 UTC (left panel) and 24 UTC (right panel, note change in scale). Shown are errors for the Northeast US based on radiosonde (circles) and NARR analysis (triangles) comparisons, for the u- (solid lines) and v-wind (dashed lines) components.

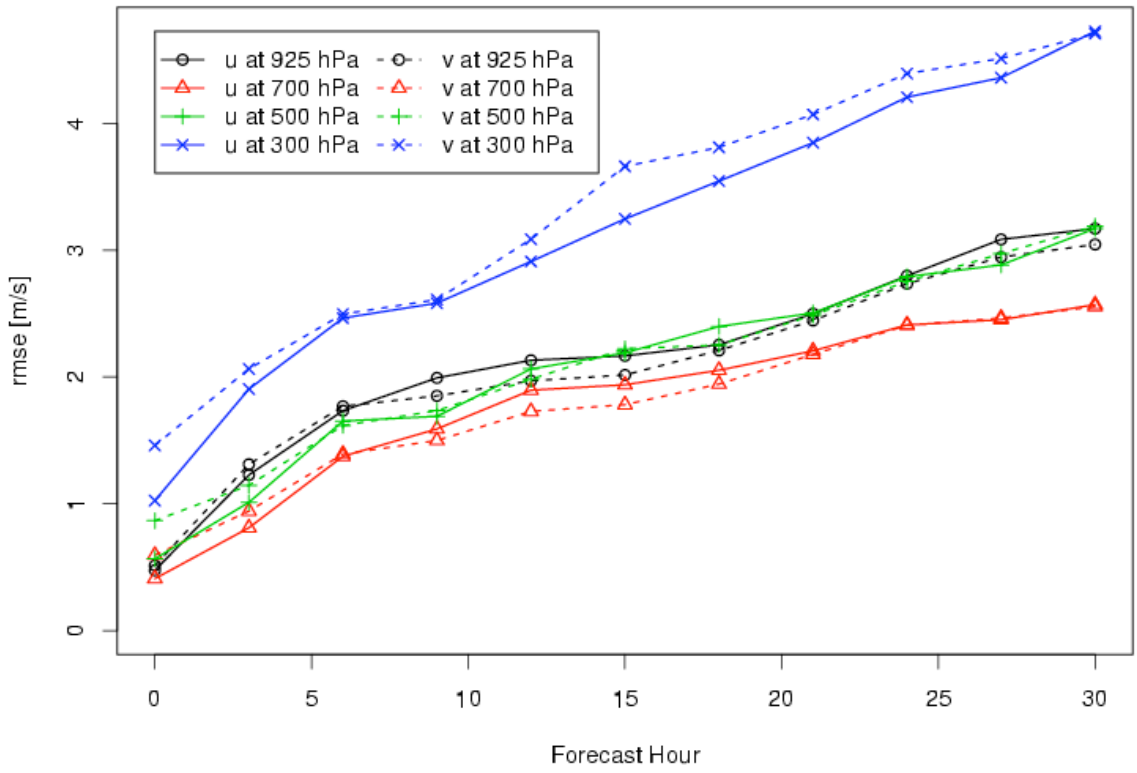

Fig. 4: Evolution of RMS forecast errors with respect to NARR analyses over the Northeast US. Errors are shown for the u- (solid lines) and v-wind components (dashed lines), at pressure levels 925 hPa (circles), 700 hPa (triangles), 500 hPa (+), and 300 hPa (x).

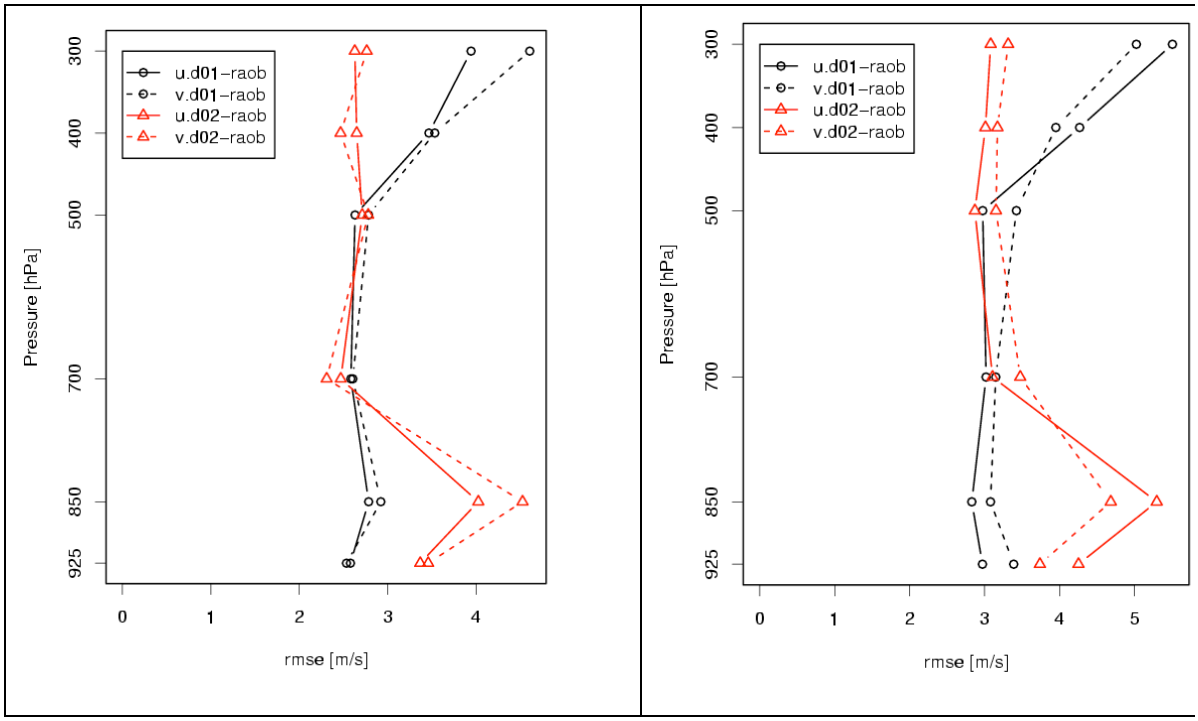

Fig. 5: As Figure 4, except for radiosonde locations over the inner domain box in Figure 2, for coarse resolution (40-km grid spacing; circles) and high-resolution (8-km grid spacing; triangles) WRF fields, for 20 days in June 2004.

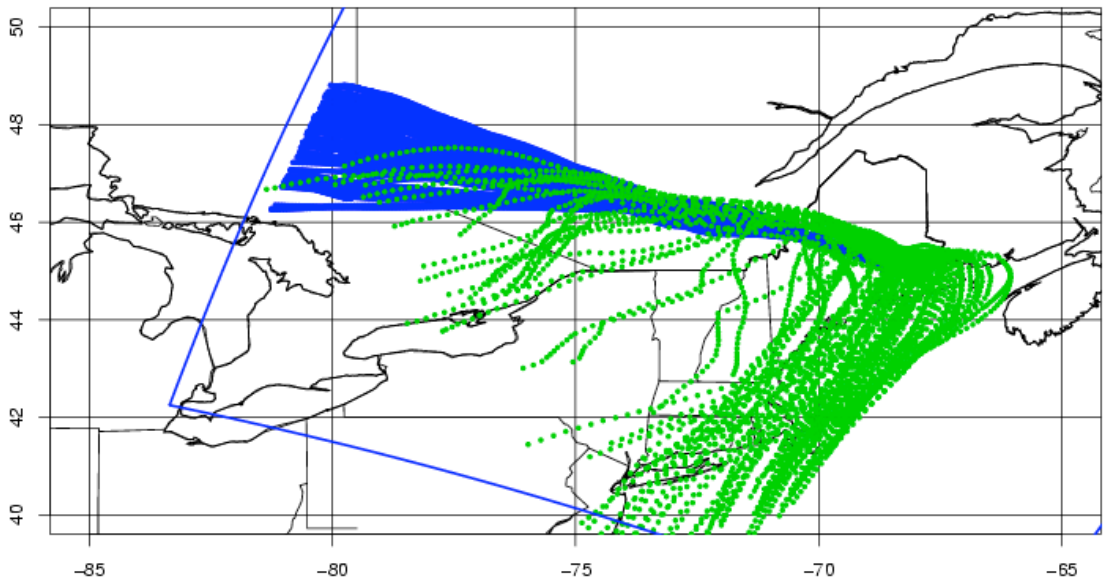

Fig. 6: Particle locations for 30-hour back trajectories from Argyle, 23 UTC 23 June 2004, using coarse resolution (green) and nested (blue) WRF model fields. The nested domain boundary is shown as a blue line.

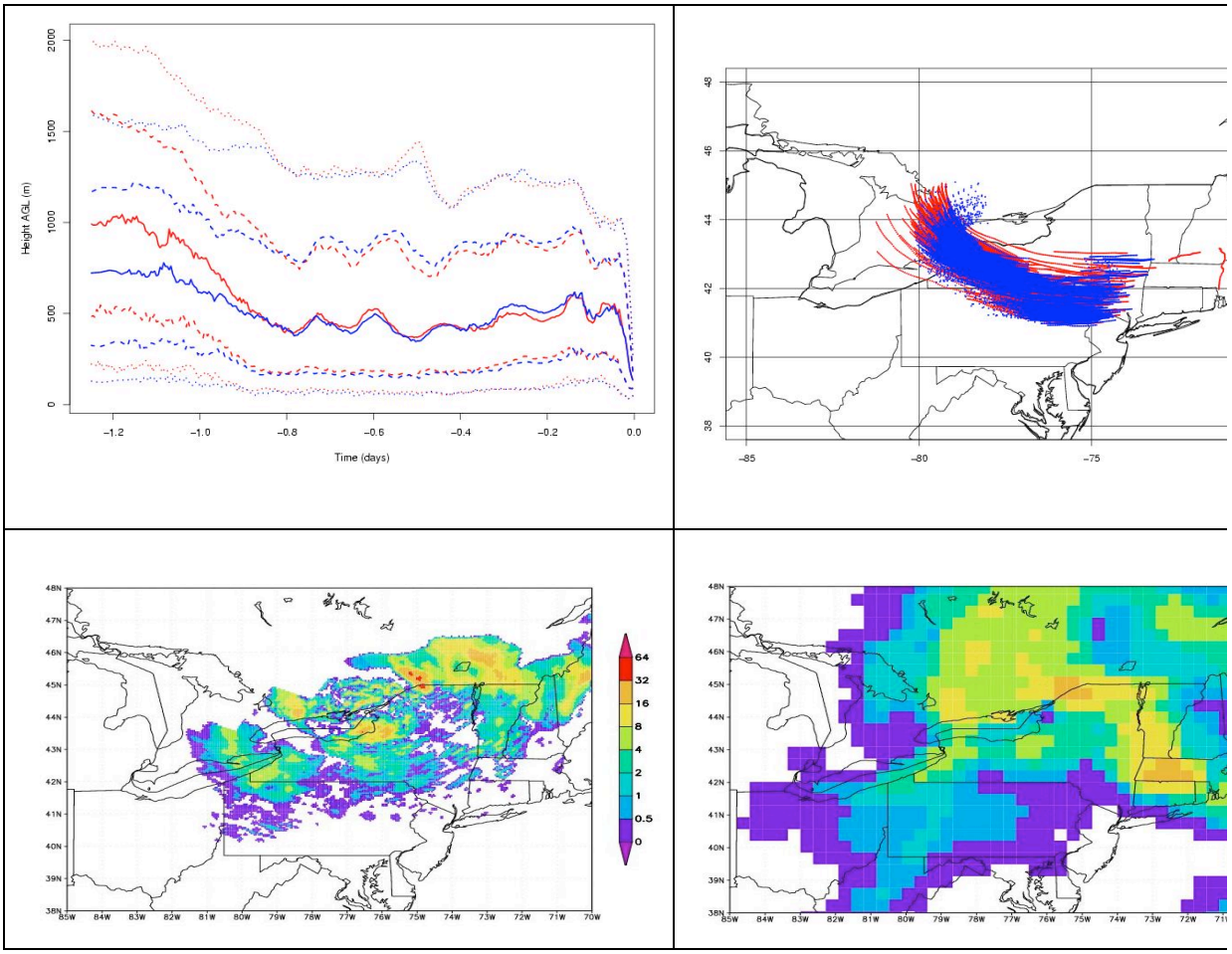

Fig. 7: Effect of convective precipitation on computed trajectories. Top left: time series of 10th and 90th (dotted), 25th and 75th (dashed), and 50th (solid) percentiles of height above ground for the particles along back trajectories beginning at 18 UTC 16 July 2004, shown in red for the case with convection, and in blue for the case without convection. Top right: Particles locations between 24 and 30 hours back trajectory time, shown in red for the convective case, and overplotted in blue for the case without convection. Bottom left: Stage IV observed precipitation (kg/m2) between 12 and 18 UTC 15 July 2004. Bottom right: WRF-predicted convective precipitation (kg/m2) between 12 and 18 UTC 15 July 2004.

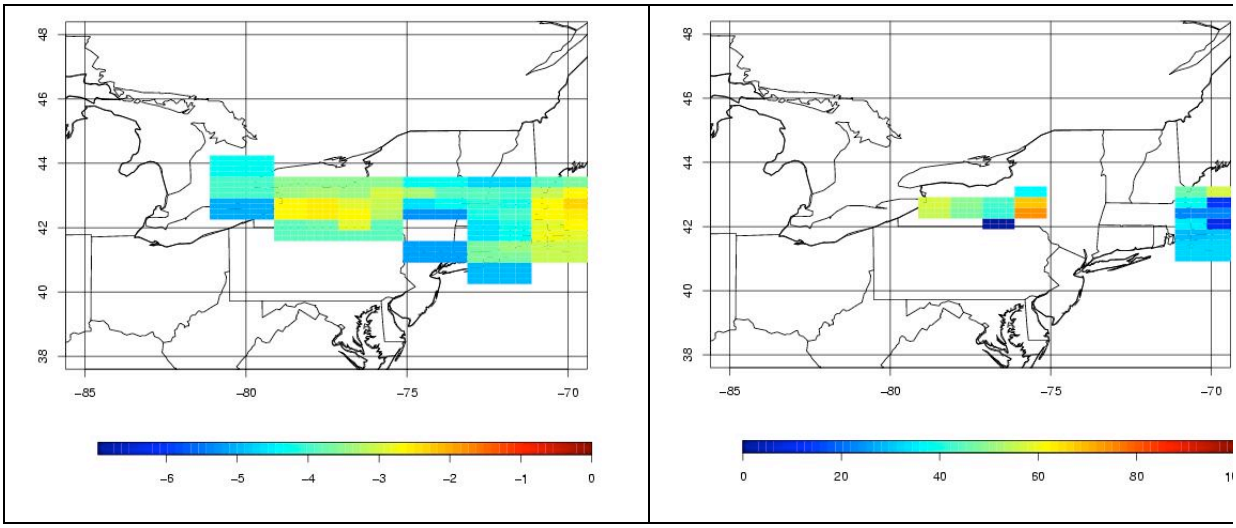

Fig. 8: Footprints for the trajectories with convection shown in Figure 7, plotted for values between 10^{-7} and 1 using a logarithmic color scale (left panel). The right panel shows the percentage difference between convective and non-convective footprints for footprints exceeding 10^{-3}.

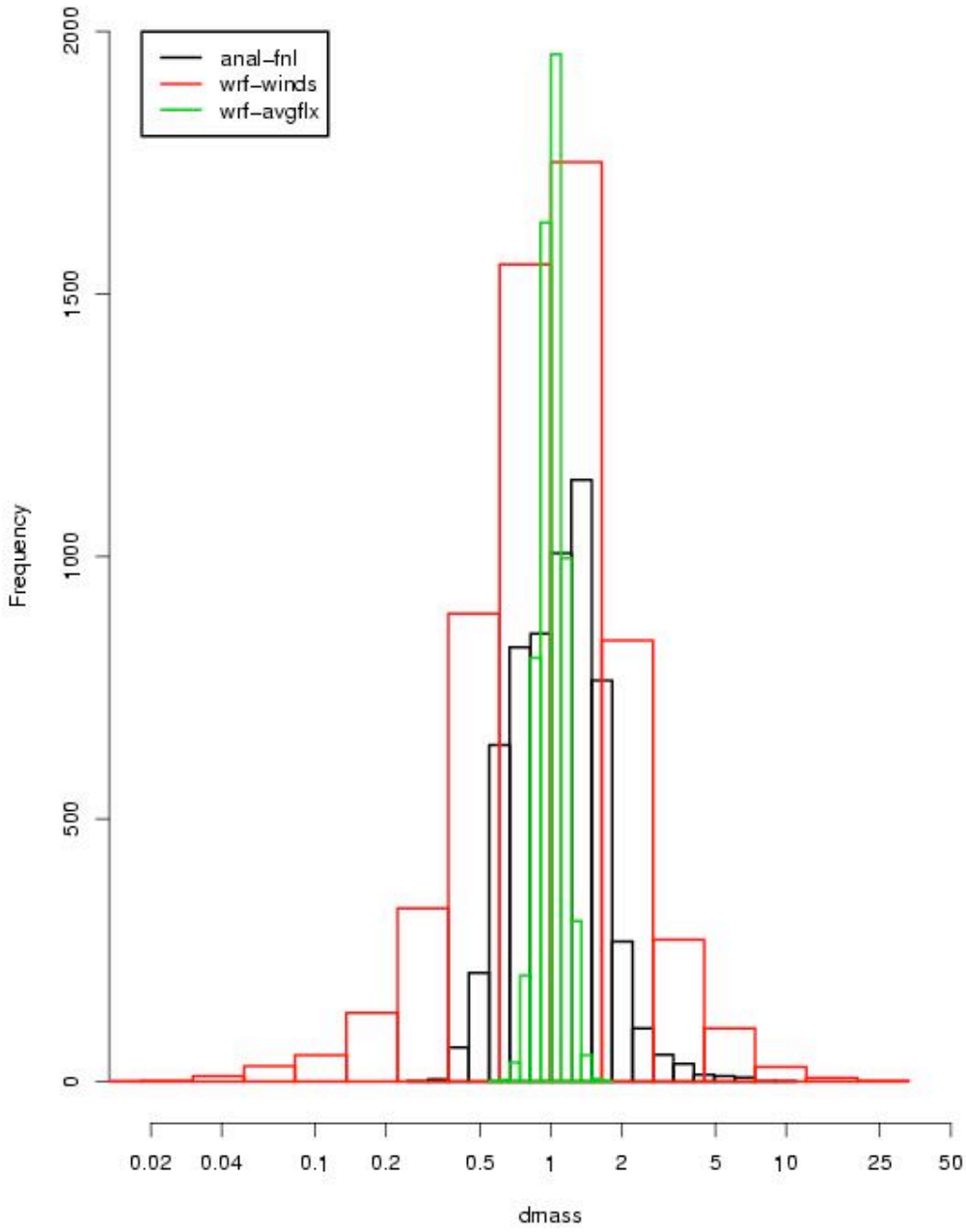

Fig. 9: Histogram of mass conservation parameter dmass at the end of two-day trajectories for 6 dates in July 2004, using global analysis fields ("anal-fnl"), and outer domain WRF instantaneous wind velocities ("wrf-winds") and time-averaged fluxes ("wrf-avgflx").

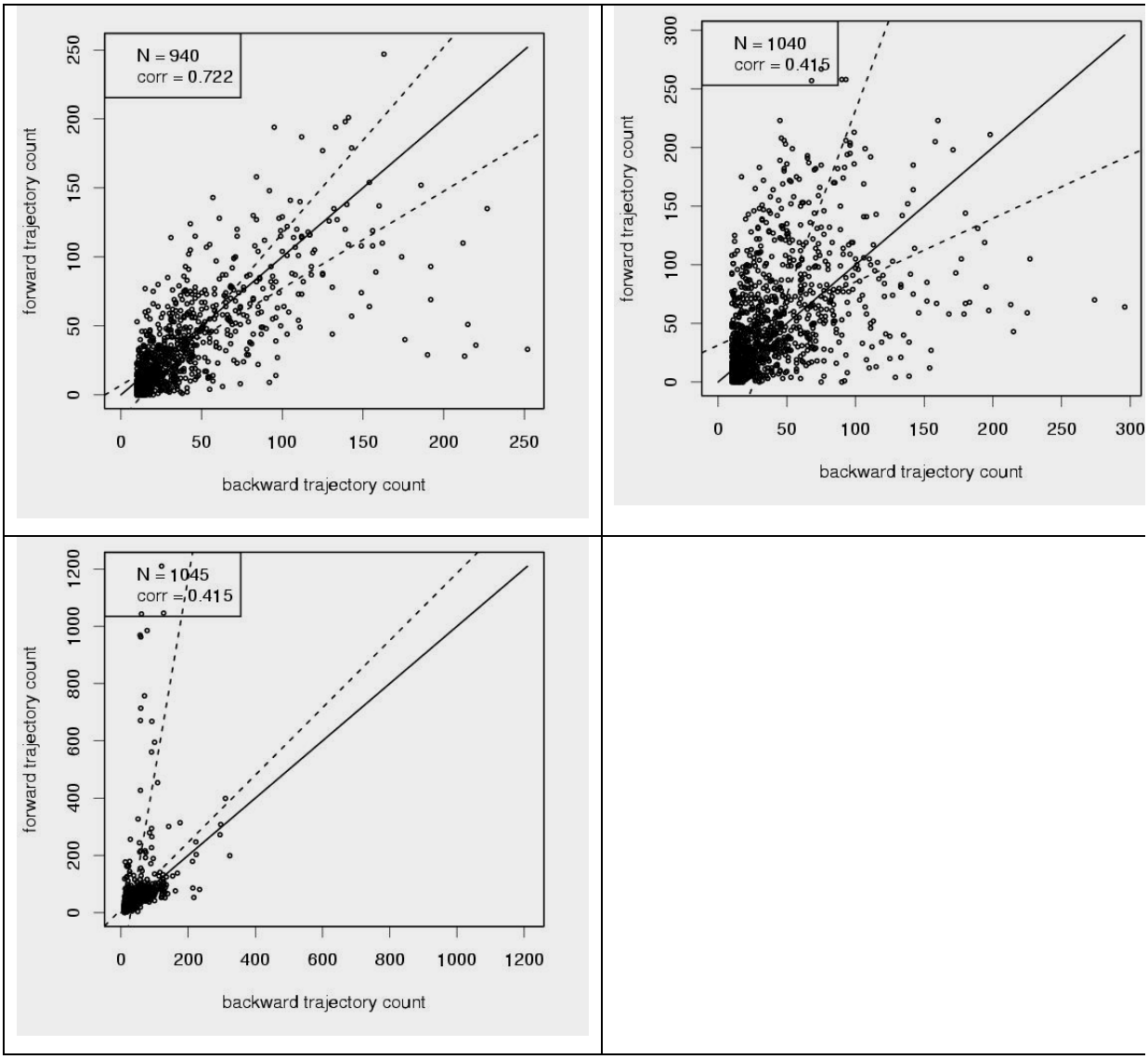

Fig. 10: Scatterplot of forward-backward trajectory particle counts. Top left: WRF time-averaged flux fields; Top right: WRF instantaneous wind fields; Bottom left: Global analysis fields. The regression lines (forward regressed against backward and vice-versa) are dashed, the 1:1 line is solid. Text box shows the number of data points in the plots, and the correlation coefficient.